Wave-solid interactions in laser-shock-induced deformation processes

Y. Fan,[a] Y. Wang, S. Vukelic, and Y. L. Yao
Department of Mechanical Engineering, Columbia University, New York, New York 10027

(Received 22 June 2005; accepted 14 October 2005; published online 30 November 2005)

A model was developed for material deformation processes induced by laser-generated shock waves. The processes include laser peen forming (LPF) and laser shock peening (LSP) of metals. Numerical solutions of the model using finite element method were implemented in two steps: (1) explicit step, devoted to shock wave propagation, and (2) implicit step, calculating relaxation of material. A series of LPF and LSP experiments was conducted to validate the model. The residual stress measurements by synchrotron x-ray diffraction and deformation measurements by profilometry showed that the experimental and numerical results were in good agreement. It is the first time to numerically and experimentally study the novel process of micro-scale LPF. An important aspect of the work is that the numerical results were further analytically explored to gain improved understanding of wave-solid interaction including shock wave attenuation and shock velocity variation. © *2005 American Institute of Physics*. [DOI: 10.1063/1.2134882]

I. INTRODUCTION

Shock waves are characterized in that the wave front, in which compression takes place, is a region of sudden and violent change in material velocity, stress, and density. Since the experiments in the 1960s utilizing high-power pulsed lasers to generate shock waves in solid targets, the laser shock technique has led to many investigations, including laser peen forming (LPF) and laser shock peening (LSP), as shown in Fig. 1.

Laser-generated shock waves result from the expansion of a high-pressure plasma caused by a pulsed laser. An intense laser pulse interacting with a solid target immediately causes the surface layer to instantaneously vaporize into a high-temperature and high-pressure plasma. This ablated plasma expands from the surface and, in turn, exerts mechanical pressure on the face of the target, which induces compressive waves in the solid target, and therefore a shock wave is propagated through the sample. If it is confined by liquid or another type of laser transparent medium, the shock pressure can be magnified by a factor 5 or more compared with the open-air condition.[1] The coating also protects the target from thermal effects so that nearly pure mechanical effects are induced. LSP is a process in which beneficial compressive residual stress is imparted into the processed surface layer of metal or alloy parts by laser-generated shocks, and the process has been extensively investigated and in some cases successfully applied.[2–7] When the peak pressure created by the shock wave is above the dynamic yield stress [Hugoniot elastic limit (HEL)] of metal, the metal is plastically deformed at the surface which will induce compressive residual stress in the surface of the part and thus increase the resistance of the metal to surface-related failures such as fatigue, fretting fatigue, and stress corrosion cracking. LSP is only a surface treatment method, and does not produce appreciable change of shape. LPF is a process involving laser-generated shock waves. It combines the beneficial effects (compressive residual stresses on the surface) of a LSP with a controlled bending deformation, to shape parts.[8,9] The process is more effective than other thermal-forming methods with a distinct advantage that surface stresses generated can be compressive. Therefore, the process results in increased fatigue resistance of the target material in addition to shaping it. However, to advance LSP and LPF, in particular, the answers to some questions, for example, how to control the repetition rate in a multiple-pulsed laser processing, how to determine the pulse duration considering the thickness of parts during LPF, and in two-sided LSP,[10] how to design the phase difference between the two shock waves in order to gain an optimal effect, need to be further investigated. These questions are closely related to the shock-solid interactions, such as shock wave attenuation and reflection and variation of shock wave velocity.

Numerical modeling is an effective way to understand shock-solid interaction. Shock wave propagation in solids has been numerically investigated.[11–15] Mok[11] simulated the propagation and attenuation of spherical and plane shock waves in a 2024 aluminum plate by assuming that the media is a strain-rate-independent and perfectly elastic plastic solid. Caruso *et al.*[12] also numerically investigated laser-generated shock propagation dynamics in the solids, but only an elastic medium in plane geometry was considered. Shock-solid interaction was also simulated in some studies of spallation and residual stresses induced by LSP,[13–15] but the effect of high strain rate was not considered or fully considered only by the Johnson-Cook law. Most studies on the shock-solid interaction provide few practical directions for the application of material deformation processes induced by laser-generated shock waves.

In this work, an explicit/implicit finite element method (FEM) model is developed to simulate material deformation processes induced by laser-generated shock waves. Explicit dynamic analysis is implemented for shock wave propagation in strain-rate-dependent and elastic-plastic solids, and implicit analysis is applied for relaxation of pressured mate-

[a]Electronic mail: yf2121@columbia.edu

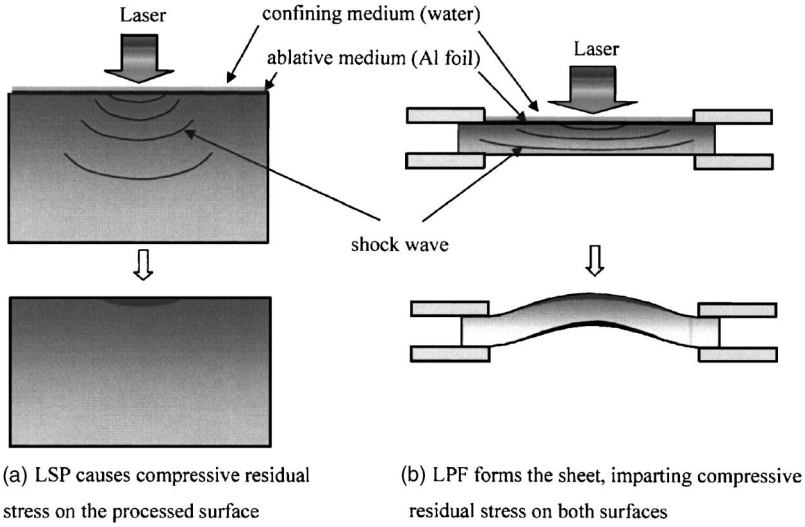

FIG. 1. Material deformation processes induced by laser-generated shock waves: (a) laser shock peening (LSP) and (b) laser peen formig (LPF).

rials. The resultant plastic deformation and residual stress fields can be then calculated. The model is validated by comparing the calculated deformation and residual stress fields with deformation measurements by profilometry and the residual stress measurements by synchrotron x-ray diffraction. The numerical results were further analytically explored to gain improved understanding of wave-solid interaction including shock wave attenuation and shock velocity variation.

II. BASIC EQUATIONS

When a high pressure is suddenly applied to a metallic target, the pressure is accumulated in the wave front because it cannot disperse away within such a short time, and the wave front becomes steeper and steeper, and finally evolves into an almost discontinuous jump. A shock wave is then formed. Because the pressure is accumulated, the shock front is highly compressive, which also causes the discontinuity of density, stress, and other quantities between shock wave front and the unshocked region. The shocked solids are thought to have a fluidlike hydrodynamic deformation under such a high pressure, but solids are still different from liquids in that solids have material strength and plastic flow, and their deformation behavior is related to strain and strain rate, in particular.

A. Laser-generated shock loading

A model was previously developed for the prediction of laser-generated pressure in the confined ablation mode.[16] It considered the mass, energy, and momentum exchanges between plasma and confining medium or plasma and metallic target. The expansion of the plasma was modeled as one-dimensional laser-supported combustion wave. Figure 2 presents the calculated laser-generated shock loading profiles under different processing conditions. The calculated shock loading was assumed to be of a spatially Gaussian distribution and would be used in the later shock wave propagation simulation as input shock loading.

B. Hydrostatic and deviatoric behaviors

The precise numerical description of a LPF or LSP process requires the simulation to take into account the hydrodynamic behavior of the material and the deviatoric behavior considering work hardening and strain rate effects. When the applied stress greatly exceeds the yield stress of a solid, material behavior is more complicated, and can be approximated by a fluidlike one because the fractional deviations from stress isotropy are small. The complete process of shock wave propagation in solids should be governed by the three conservation equations,[17] equation of state that can be expressed in terms of specific internal energy as a function of pressure and density for the hydrodynamic behavior of the material, and the elastic-plastic constitutive relation for deviatoric behavior.

In the calculation of the elasto-plastic behavior, the stress-tensor components are divided into a hydrostatic equation of state and an elastic-plastic constitutive model. The stress components σ_{ij} can be written as

$$\sigma_{ij} = -P + s_{ij}, \tag{1}$$

where P is the hydrostatic pressure and s_{ij} is the deviatoric stress components.

A commonly used equation of state for solids is the Mie-Grüneisen equation of state.[18] The Mie-Grüneisen equation

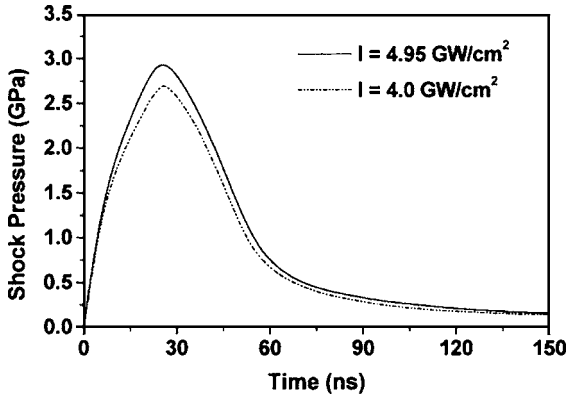

FIG. 2. The loading history based on a former model.

of state, which establishes relationship between pressure P and internal energy E with reference to the material Hugoniot curve, was used,[18]

$$P - P_H = \gamma_0 \rho_0 (E - E_H), \tag{2}$$

where P_H and E_H are the Hugoniot pressure and internal energy, γ_0 is a material constant, and ρ_0 represents the initial-state density.

The Hugoniot curve is described by the linear relation between the shock velocity U and particle velocity u with coefficients from experimental data,[19]

$$U = C_0 + Su, \tag{3}$$

where the constant C_0 is the sound speed at zero pressure, and the material constant s has a value between 1.0 and 1.7 for most metals.

Combining Eq. (6) with the Rankine-Hugoniot jump conditions,[20] the Hugoniot pressure and internal energy can be obtained as

$$P_H = \frac{\rho_0 C_0 \eta}{(1 - S\eta)^2}, \tag{4}$$

$$E_H = \frac{P_H \eta}{2\rho_0}, \tag{5}$$

and substituting Eqs. (7) and (8) into Eq. (5) yields the following:

$$P = \frac{\rho_0 C_0 \eta}{(1 - S\eta)^2}\left(1 - \frac{\gamma_0 \eta}{2}\right) + \gamma_0 \rho_0 E, \tag{6}$$

where $\eta = 1 - \rho_0/\rho$, and ρ is the density. Equation (6) is the final form of the equation of state to be used in this simulation. In the following numerical modeling of shock-solid interactions, work hardening, strain rate, and pressure effects on yield strength are considered while temperature is taken as room temperature. This is reasonable because only the coating is vaporized and minimal thermal effects are felt by the sample. The solid target is assumed to be isotropic.

III. NUMERICAL MODELING

A. FEM explicit and implicit modelings

The commercial finite element solvers, ABAQUS/Explicit and ABAQUS/Standard, were combined to perform the LSP and LPF simulation. These two solvers accomplish different calculations during this simulation. The ABAQUS/Explicit is a nonlinear explicit time integration finite element code, which is especially well suited for solving high-speed, short-duration, highly dynamic events that require many small time step increments to obtain a high-resolution solution.[21] The element type is CPE4R in modeling of LPF, and CAX4R in modeling of LSP. Fine elements were used to model the area around the shock load, and the elements were biased laterally and vertically away from the load center. The finest grid is around 0.4 μm. One important issue about the simulation of LPF and LSP is the balance between a short time for dynamic shock-solid interaction (two to three times of the laser-pulse duration) and a much longer relaxation time (up to 1 s) to reach a stabilized mechanical state. So the ABAQUS/Explicit code is first applied to simulate the dynamic shock-solid interaction process. But the ABAQUS/Explicit method is only conditionally stable and a very small time step is required. Therefore, the second step is to simulate material relaxation in ABAQUS/Standard. As soon as the calculation of the highly dynamic shock-solid interaction process is completed in ABAQUS/Explicit, the obtained intermediate stress and strain state is transferred into ABAQUS/Standard to simulate the material relaxation and get the residual stress filed in static equilibrium.

B. Strain-rate-dependent considerations

In LPF and LSP, the target is subjected to very strong shock pressures (>1 GPa), the interaction time is very short (<200 ns), and the strain rate is very high (>100 000 s^{-1}). It is necessary to consider the effect of high strain rate on the flow behavior of metals. Johnson *et al.*[22] first included the influence of strain rate $\dot{\varepsilon}$ into their working hardening model. But the model of Johnson *et al.*[22] could not cover the high strain rate (greater than 10^{-6} s^{-1}) in LPF and LSP. It did not also consider pressure effects, which are very important in laser shock processing. The model of Steinberg *et al.*[23] is applicable to ultrahigh pressures but it did not consider rate-dependent effects. It was found that the rate-dependent effects cannot be neglected for shock pressures below 10 GPa. In laser shock processing, the pressure involved is fairly high (>1 GPa) but less than 10 GPa.

For laser shock processing, therefore, both the strain rate effects and ultrahigh pressure effects on material yield stress need to be considered. A prior research[5] has proposed a model including the strain rate (even above 10^6 s^{-1}) effects and ultrahigh pressure effects on material yield stresses, and predicted the laser shock peening processes very well. The obtained dynamic yield stress data from the prior research[5] were used in this work.

IV. EXPERIMENTS

A. Laser and sample preparations

All experiments were made by a frequency-tripled Q-switched Nd: yttrium aluminum garnet (YAG) laser with a wavelength of 355 nm in TEM_{00} mode. The pulse duration was 50 ns, and the pulse repetition rate could vary between 1 and 20 kHz. The laser beam diameter is 12 μm and the laser intensity was varied from 2 to 6 GW/cm^2.

For LPF, copper stripes with a thickness of 100 μm were used as samples. These stripes were cut to 20×3 mm^2 using a wire electric discharge machine (EDM), and then heat treated and electropolished to relieve residual stress. Then, a thin layer of high-vacuum grease (about 10 μm) was spread evenly on the polished sample surface, and the ablative medium, aluminum foil of 16 μm thick, was tightly pressed onto the grease. These stripes were clamped at both ends, leaving 10 mm length in the middle unsupported for LPF experiments. Caution was exercised to prebending effects and to ensure that these stripes remain flat during these steps.

For LSP, well-annealed pure aluminum samples in the dimensions of $15 \times 10 \times 5$ mm^3 were used. The sample

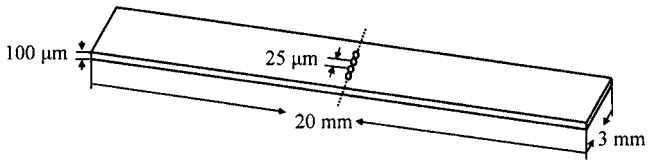

FIG. 3. Schematic of the laser irradiation scheme in LPF.

preparation was the same as introduced before.[3] The setups for LPF and LSP are schematically shown in Fig. 1.

For both LPF and LSP, the laser process procedure is similar. The samples were placed in a shallow container filled with distilled water around 3 mm above the sample top surface. A series of laser pulses was applied along the width direction (the dimension of 3 mm for LPF and the dimension of 10 mm for LSP) with 25 μm spacing between adjacent pulses. This forms a about uniformly deformed straight shocked line (Fig. 3). Pulse energies of 226 and 280 μJ corresponding to laser intensities of 4.0 and 4.95 GW/cm^2 were used for LPF and LSP, respectively. After shock processing, the coating layer and the vacuum grease were solved in acetone solution, and the shock-induced deformation and residual stresses on the samples were measured. The conditions and the mechanical properties of the studied materials are summarized in Tables I and II, respectively.

B. Deformation and residual stress measurements

Before and after LPF, the curvatures of the stripes were measured by a profilometer, and the bending caused by LPF is the net effect, as shown in Fig. 4. After LSP, the dented surface was measured using atomic force microscopy (AFM).

The residual stresses were measured by synchrotron x-ray diffraction. Synchrotron x-ray diffraction can make accurate residual stress measurement of a high spatial resolution because it provides high-brightness x-ray beams. The extremely high-brightness x-ray beams from synchrotron radiation sources are narrowed down and then focused to micron or submicron spot sizes using x-ray optics such as the Fresnel zone plates (FZPs) or tapered glass capillaries, and either white beam or monochromatic x rays can be used. The tapered capillary tube is aligned to take in the x-ray beam from the synchrotron beamline, and successively focuses the beam to a small spot size by total external reflection. Both small spot size and increased intensity are desired in x-ray diffraction with a micron-level spatial resolution. In the experiments, the capillary with an exit bore diameter of approximately 3 μm was used, and the beam spot size is an ellipse with minor and major radii of around 5×7 μm^2, respectively.

TABLE I. Samples and experimental conditions for LPF and LSP.

	Material	Sample size (mm^3)	Laser intensity (GW/cm^2)	Pulse energy (μJ)
LPF	Pure copper	$10\times3\times0.1$	4.95	280
LSP	Pure aluminum	$15\times10\times5$	4.0	226

TABLE II. Mechanical properties of the studied materials.

	ρ_0 (kg/m^3)	G (MPa)	γ	C_0 (m/s)	S
Cu	9860	468	1.99	3940	1.489
Al	2700	262	2.0	5386	1.34

The samples are mounted on a translation stage with positioning accuracy of ±1 μm in the x and y directions in the sample surface. Monochromatic synchrotron radiation at 8.0 keV ($\lambda=1.540\,24$ Å) is used, since it is smaller than the K absorption edges for Al and Cu which are 8.98 and 8.3 keV so that the fluorescence radiation would not be excited.

Multiple measurement points were chosen along a line perpendicular to the shocked line. The spacing between adjacent measurement points starts from 20 μm (when ±100 μm away from the center of the shocked line) and reduces to 5 μm within ±20 μm from the center of the shocked line in order to spatially resolve the residual stress. At each position, the corresponding x-ray-diffraction profile is recorded and repeated for each shocked line. For LSP, only the shocked surface was measured while for LPF, residual stress measurements on both top and bottom surfaces were conducted. It should be noted that the penetration depths of x ray in copper is about 10 μm and in aluminum around 40 μm. Therefore, the measured residual stress is an average in the depth.

V. RESULTS AND DISCUSSIONS

A. Model validation

1. Comparison with experimental results

The comparison between the measured deformation of the copper stripe after LPF and the numerical result predicted is shown in Fig. 4. Before laser peen forming, the stripe slightly curves upward with the center of the stripe up by about 5 μm. After LPF, the stripe bended upward further, and the shocked area was raised by up to 10 μm. The numerically predicted deformation and the experimental results are in good agreement.

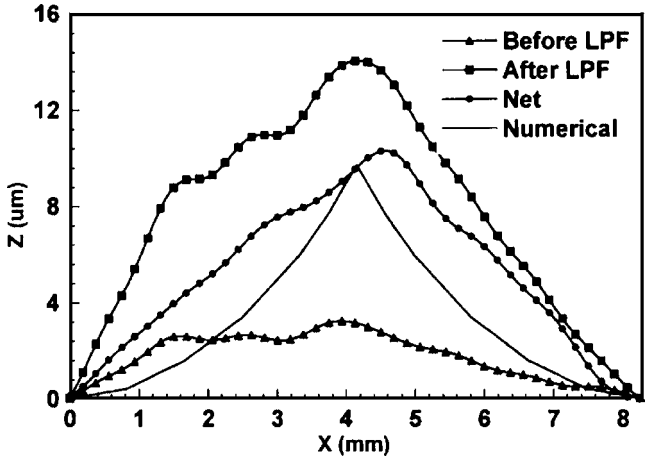

FIG. 4. Comparisons of the deformation after LPF between the experimental and the numerical results.

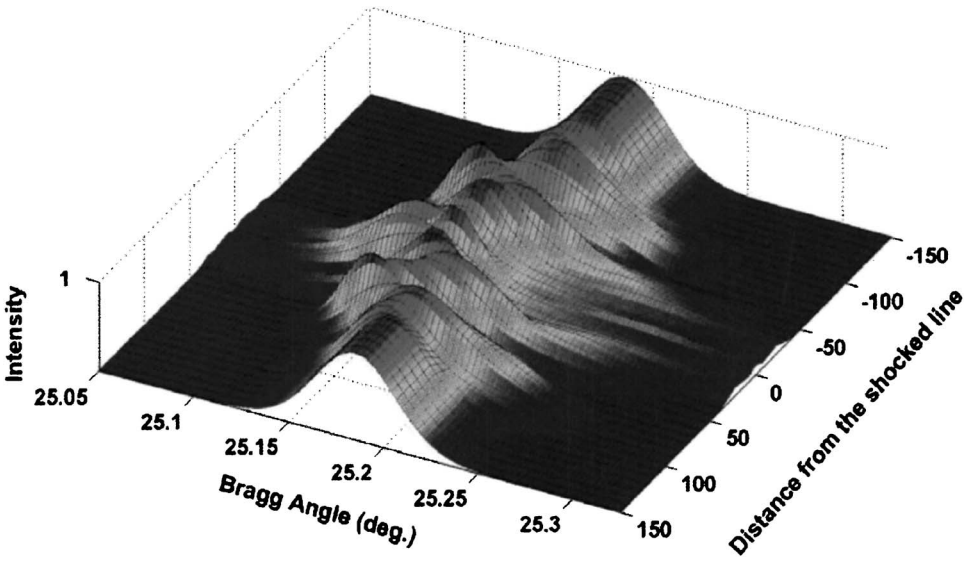

FIG. 5. Three-dimensional x-ray profile spatial distribution across the shocked line for (002) reflection of the copper sample: distance from the shocked line center in micrometers.

Figure 5 recorded x-ray-diffraction profiles along a line perpendicular to the shocked line. In Fig. 5, when the measured location is far from the shocked line (>100 μm or <-100 μm), the x-ray-diffraction profile is single symmetric peak, and the measured Bragg angle is around 25.16°, the theoretical Bragg angle for Cu (002) reflection, which indicates that the measured location is within the shock-free regions. When the measured location gets closer to the shocked line, the peak shifts towards smaller diffraction angles, meanwhile, the x-ray-diffraction profile is broadened or a second peak pops up towards larger diffraction angle. The full width at half maximum (FWHM) of the profile around the shocked line is up to three times greater than that of the line profile at 100 μm away from the center. It is known that when both elastic and plastic strains are superposed in plastically deformed metals, diffraction is both shifted and broadened.[24] It is the superposition that makes it difficult to evaluate the local strain and residual stress distribution. However, on the basis of a composite model,[25] local strain and residual stress can be evaluated for metals under plastic deformation by recognizing that the crystal dislocations often arrange themselves in a cell structure after being subjected to a shock loading. In the model, the deformed crystal is considered as a two-component system, where the local flow stress of the cell walls is considerably larger than the local flow stress of the cell interiors. Consequently, in the plastically deformed and unloaded crystals the cell walls parallel to the compressive axis are under a residual uniaxial compressive stress $\Delta\sigma_w<0$ and the cell interior under a uniaxial tensile stress $\Delta\sigma_c>0$. The asymmetrical Bragg reflections can be separated into the sum of two symmetrical peaks which correspond to "cell interiors" and "cell walls" as postulated by Ungar *et al.*[25] The centers of both components are shifted in opposite directions in accordance with $\Delta\sigma_w<0$ and $\Delta\sigma_c>0$. Then, the measure of the residual stresses can be characterized by the absolute value of the difference in the following:

$$\sigma_{zz}=|\Delta\sigma_w-\Delta\sigma_c|. \tag{7}$$

The lateral residual stress in the sample surface plane is

$$\sigma_{xx}=\sigma_{yy}=-\sigma_{zz}\nu, \tag{8}$$

where ν denotes Poisson's ratio. Following the analysis method above for each measurement point, the spatially resolved residual stress distributions on both top and bottom are shown in Fig. 6. The comparisons of the residual stress distributions on both top and bottom show that the numerically predicted distribution matches the experimental results very well. The modeled residual stress distribution and the bending induced by LPF of the copper stripe are also shown in Fig. 7. When high pressure was applied to the copper, the shocked material tended to flow away from the shocked center and caused elongation of the top layer of the stripe, which led the stripe to bend up, and meanwhile induced compressive residual stress on the bottom surface and, because of spring back and shock compression, the top surface.

Figure 8 shows that the comparison between the AFM-measured dent on the shocked area after LSP of the bulk aluminum sample and the FEM calculated. The x-ray-microdiffraction-measured residual stress distribution induced by LSP and the numerically obtained residual stress field are showed in Fig. 9. The calculated residual stresses for comparison in Figs. 6 and 9 are average in the penetration depth of x ray. Both Figs. 8 and 9 show a good agreement between the experimental and the numerical results.

2. Steady shock structure

The peak pressure of a laser-generated shock loading applied for LPF and LSP is generally in the range from 1 to 10 GPa, which is in the elastic-plastic shock regime. The elastic-plastic shock regime is characterized by a two-wave structure with an elastic precursor followed by a plastic wave, which further compresses the material to the final state. The transition from an elastic precursor to the following plastic wave occurs within a thin layer, which is also called the plastic shock front, where the material rapidly deformed. The two-step shock wave profile has been verified by a series of experiments.[26,27] To numerically obtain a steady planar shock wave, a uniform 2.0 GPa pressure loading with a duration time of 50 ns is applied. Figure 10 shows

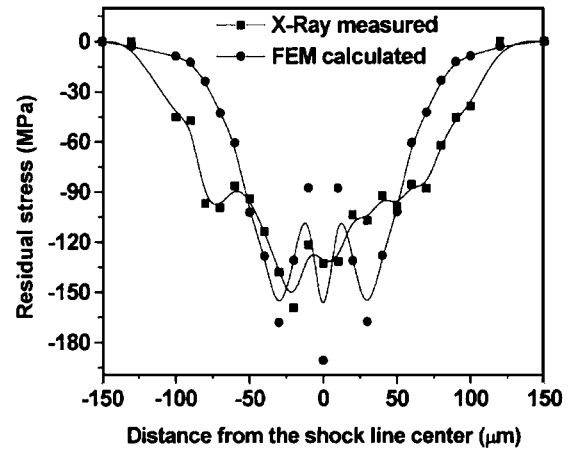

FIG. 6. Comparison between the experimental and the numerical residual stresses induced by LPF of copper stripes with a thickness of 100 μm: (a) top surface and (b) bottom.

that the calculated shock wave profiles at 50 and 100 ns. When $t=50$ ns, unloading just starts, so there is no release wave; when $t=100$ ns, a steady shock wave with a release wave moving in the same direction is obtained, and both shock front and release wave are characterized by elastic and plastic responses with a two-step profile. The numerically obtained steady shock wave structure matches the theoretical and experimental analyses made by Lipkin and Asay.[27]

The above comparison and wave profile analysis demonstrate that the proposed numerical method is a satisfactory one for solving shock-solid interaction problems. Based on the model, shock wave velocity variation, attenuation, and effect of strain rate are then further explored.

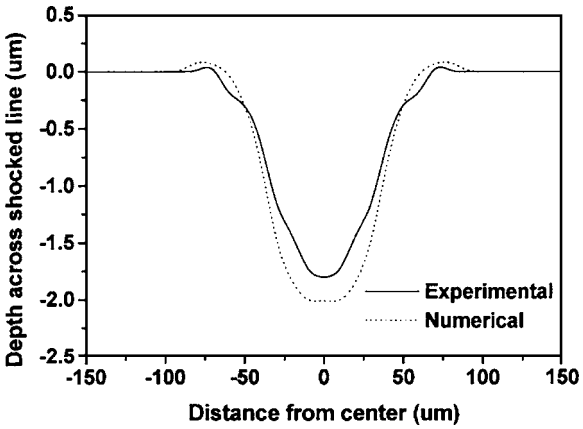

FIG. 8. Comparison of the measured and simulated dents across the shocked line after LSP of the Al sample.

B. Shock wave velocity variations

It is well known that the shock wave velocity in solids is relative to stress or pressure. During shock wave propagation in a metal plate, the shock velocity varied as the changing stress states. A one-dimensional shock wave motion is considered. The governing equations in Lagrangian form are

$$\rho_0 \frac{\partial u}{\partial t} = \frac{\partial \sigma}{\partial X}, \quad \text{(momentum conservation)}$$

$$\frac{\partial u}{\partial X} = \frac{\partial \varepsilon}{\partial t}, \quad \text{(mass conservation)} \tag{9}$$

where X is the Lagrangian displacement, and σ and ε are the stress and strain, respectively.

Assuming a stress-strain constitutive relation $\sigma=\sigma(\varepsilon)$, neglecting the effect of strain rate, and that particle velocity u is a single-valued function of σ, Eq. (9) can be rewritten as

$$\rho_0 \frac{\partial u}{\partial \sigma}\frac{\partial \sigma}{\partial t} - \frac{\partial \sigma}{\partial X} = 0,$$

$$\frac{\partial u}{\partial \sigma}\frac{\partial \sigma}{\partial X} = \frac{\partial \varepsilon}{\partial \sigma}\frac{\partial \sigma}{\partial t}. \tag{10}$$

Solving Eqs. (10) yields

$$\rho_0 \left(\frac{\partial u}{\partial \sigma}\right)^2 = \frac{\partial \varepsilon}{\partial \sigma}. \tag{11}$$

Based on Eq. (11), a characteristic speed of propagation can be expressed as

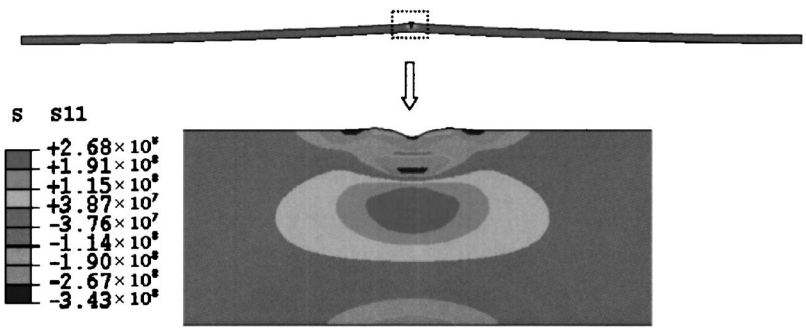

FIG. 7. The simulated deformation and residual stresses field induced by LPF. The deformation of the stripe is magnified by ten times for viewing clarity.

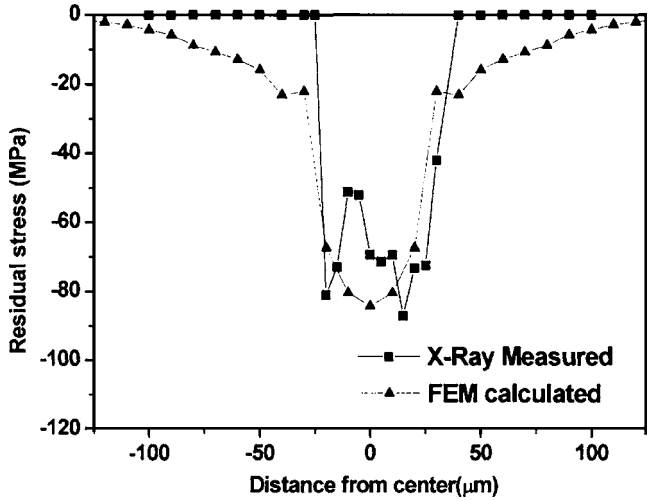

FIG. 9. Comparison between the measured residual stresses distribution induced by LSP on the shocked surface of the Al sample with the numerical result.

$$U(\sigma) = \frac{1}{\rho_0 \partial u/\partial \sigma} = \sqrt{\frac{1}{\rho_0}\frac{\partial \sigma}{\partial \varepsilon}}. \tag{12}$$

If the shock wave is a linear elastic wave, the wave speed is constant based on Eq. (12). For a typical shock wave in LSP or LPF, the stress-strain constitutive relation is more complicated considering plastic deformation and work hardening. According to the Johnson-Cook law, an elastic-plastic constitutive relation, including effects of work hardening and strain rate, can be expressed as

$$\sigma = (A + B\varepsilon^n)\left[1 + C \ln\left(\frac{\dot{\varepsilon}}{\dot{\varepsilon}_0}\right)\right], \tag{13}$$

where A, B, C, and n are material constants (for example, $A=120$ MPa, $B=300$ MPa, $n=0.35$, and $C=0.1$ for pure aluminum), ε is equivalent plastic strain, and $\dot{\varepsilon}$ and $\dot{\varepsilon}_0$ are strain rate and the strain rate under quasi-static loading. If the strain rate effect is neglected, Eq. (13) can be rewritten as

$$\sigma \approx (A + B\varepsilon^n). \tag{14}$$

Substituting Eq. (14) into Eq. (12) leads to

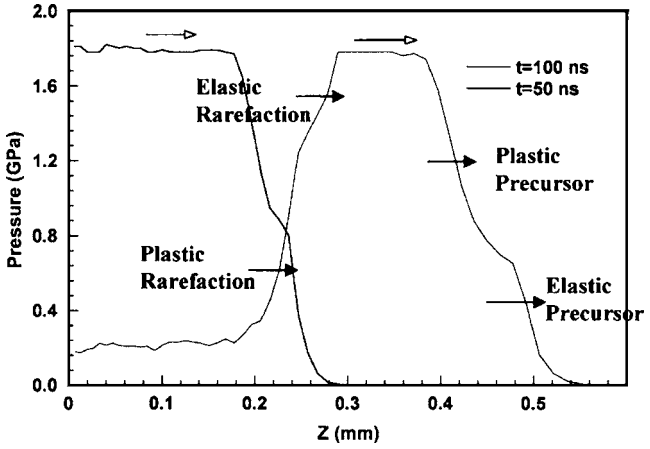

FIG. 10. The numerically obtained structure of the steady shock wave: laser pulse duration time=50 ns.

$$U(\varepsilon) = \frac{1}{\rho_0 \partial u/\partial \sigma} = \sqrt{\frac{1}{\rho_0}\frac{\partial \sigma}{\partial \varepsilon}} = \sqrt{\frac{Bn}{\rho_0}\varepsilon^{n-1}}. \tag{15}$$

Because n is smaller than unity and B is positive for most metals, Eq. (15) shows that the wave velocity varies with strain: The larger the strain is, the smaller the shock wave velocity.

To investigate the variation of shock wave velocity during propagation, the simulation of a planar shock wave propagating in a copper plate with a thickness of 1.6 mm and a length of 10 mm is run based on this proposed model under plane strain condition. A uniform 2.0 GPa pressure loading with a duration time of 50 ns is applied to produce a planar shock wave, while a Gaussian-distributed pressure loading with a small effective radius of 0.5 mm and the peak pressure of 2.0 GPa are exerted on the top surface of the copper plate with a radius of 5 mm to get a spherical shock wave by the proposed model with axis-symmetric condition. Figure 11 shows the simulated planar shock wave and spherical shock wave. Figure 12 shows the calculated stress history at $Z=0.4$ mm (1/4 thickness), $Z=0.8$ mm, and $Z=1.2$ mm of the copper plate for both planar shock and spherical shock cases. From Fig. 12, the average shock velocity within each 1/4 of thickness can be calculated in terms of the time cor-

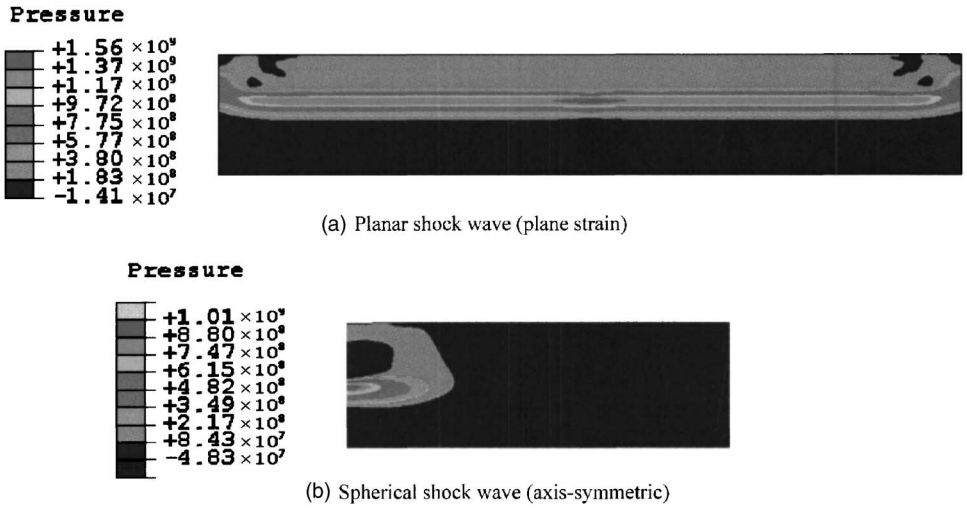

FIG. 11. The simulated shock waves: (a) planar shock wave and (b) spherical shock wave.

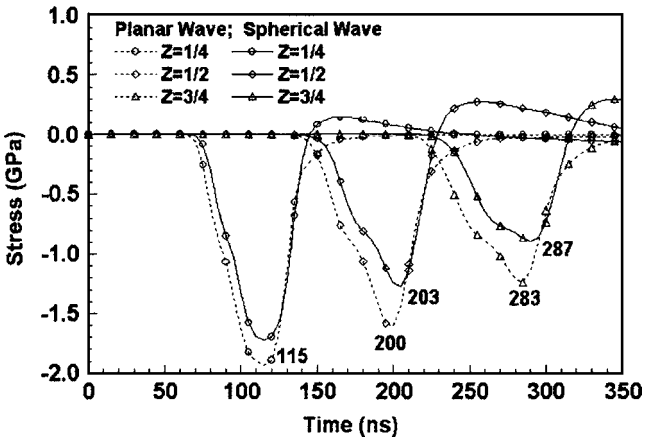

FIG. 12. The calculated time history of the stress at three locations below the shocked surface. (X=0 mm) along the thickness direction for both the planar shock wave and the spherical shock wave.

responding to the peak stress at those locations. For the planar shock, the average plastic wave velocity within the first 0.4 mm is about 4.4 km/s [=0.4 mm/(115–25 ns), 25 ns is half of the pressure duration time], 4.7 km/s [=0.4 mm/(200–115 ns)] within the second 0.4 mm, and 4.8 km/s [=0.4 mm/(283–200 ns)] within the third 0.4 mm. For spherical shock wave, it is also shown that the plastic wave speed increases as it is propagating. Comparing the plastic wave speed of the planar wave with that of the spherical wave, it is found that they are the same within the first 0.4 mm, and later on the spherical wave propagates faster than the planar wave. This can be explained by Eq. (15). Equation (15) shows that the larger the strain is, the smaller the shock wave velocity. The calculated peak plastic strain along the thickness of the copper plate is shown in Fig. 13, which demonstrates a decreasing equivalent peak plastic strain, therefore based on Eq. (15), the plastic wave speed increases. Moreover, Fig. 13 shows that the equivalent peak plastic strain within the initial 0.2 mm in the planar wave propagation is larger than that in the spherical shock propagation, and after that it becomes less due to greater strain rate hardening, which also explains why the spherical wave propagates faster than the planar wave after the first 0.4 mm.

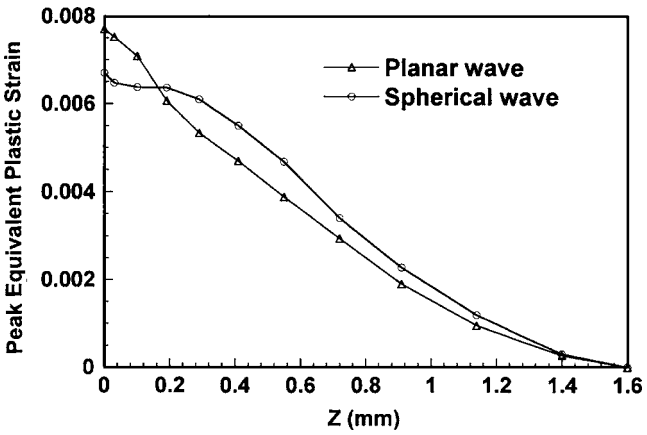

FIG. 13. The calculated peak equivalent plastic strain along the thickness of the copper plate.

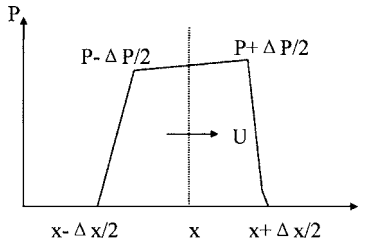

FIG. 14. Schematic of a single centered shock wave.

C. Attenuation of planar and spherical shock waves

For a LSP process as a surface treatment method, the thickness of part is generally large compared with the treated area and the part is thus often thought to be a semi-infinite body and in this case, the driven shock wave in a LSP is assumed to be spherical. Here a spherical wave is just a wave which propagates about radically, and is not strictly by definition. While for a LPF process, the sheet has a smaller thickness relative to laser spot size to be formable, therefore the driven shock wave in LPF can be reasonably assumed to be planar wave. As informed before, the shock wave attenuations directly determine the selection of some processing parameters, such as pulse duration time and duty cycle in laser processing involving multiple pulses.

Assuming a centered single shock wave is propagating, as shown in Fig. 14. The center of the shock wave is at x with pressure P, and the leading and tailing edges of the shock are at $(x+\Delta x/2)$ and $(x-\Delta x/2)$ with pressures $(P+\Delta P/2)$ and $(P-\Delta P/2)$, respectively. The width of the shock wave at x is Δx. Based on the above assumptions, when the shock wave propagates for a short distance from x_0 to x, the following attenuation of particle velocities of the planar shock wave and the spherical shock wave can be expressed as (the derivation is given in Appendix):

$$\frac{u(x)}{u(x_0)} = \exp[-K_P(x-x_0)] \quad \text{(planar wave)}, \tag{16}$$

$$\frac{u(x)}{u(x_0)} = \frac{x_0}{x}\exp[-K_S(x-x_0)] \quad \text{(spherical wave)}, \tag{17}$$

where $\Delta P = P(x+\Delta x/2) - P(x-\Delta x/2)$ and $K_S = K_P = 1/2\Delta x(\partial U/\partial P)\Delta P/U$. When the shock wave moves from x_0 to x, we have $(x_0/x > 1)$. Comparing Eqs. (16) and (17), it is found that the spherical wave decays faster than the planar wave under the same conditions due to greater geometrical dissipation of energy. Additionally, in the case of small impacts driving to spherical shock waves, the faster attenuation also comes from lateral release waves generated at the edges of impacts. The interaction between lateral release waves and longitudinal shock wave occurs earlier when the impact radius is small. Therefore, comparing LPF of a thin plate in which a planar shock wave is assumed to generate, with LSP of a thick plate in which the laser-driven shock is thought to be spherical wave, the pulse repetition rate in LPF should be lower than that in LSP. In addition, attenuation of planar wave and spherical wave is also relative to the value of K_S or K_P. $\partial U/\partial P > 0$ is a necessary condition to form a shock wave and its value is only dependent on the elastic property and

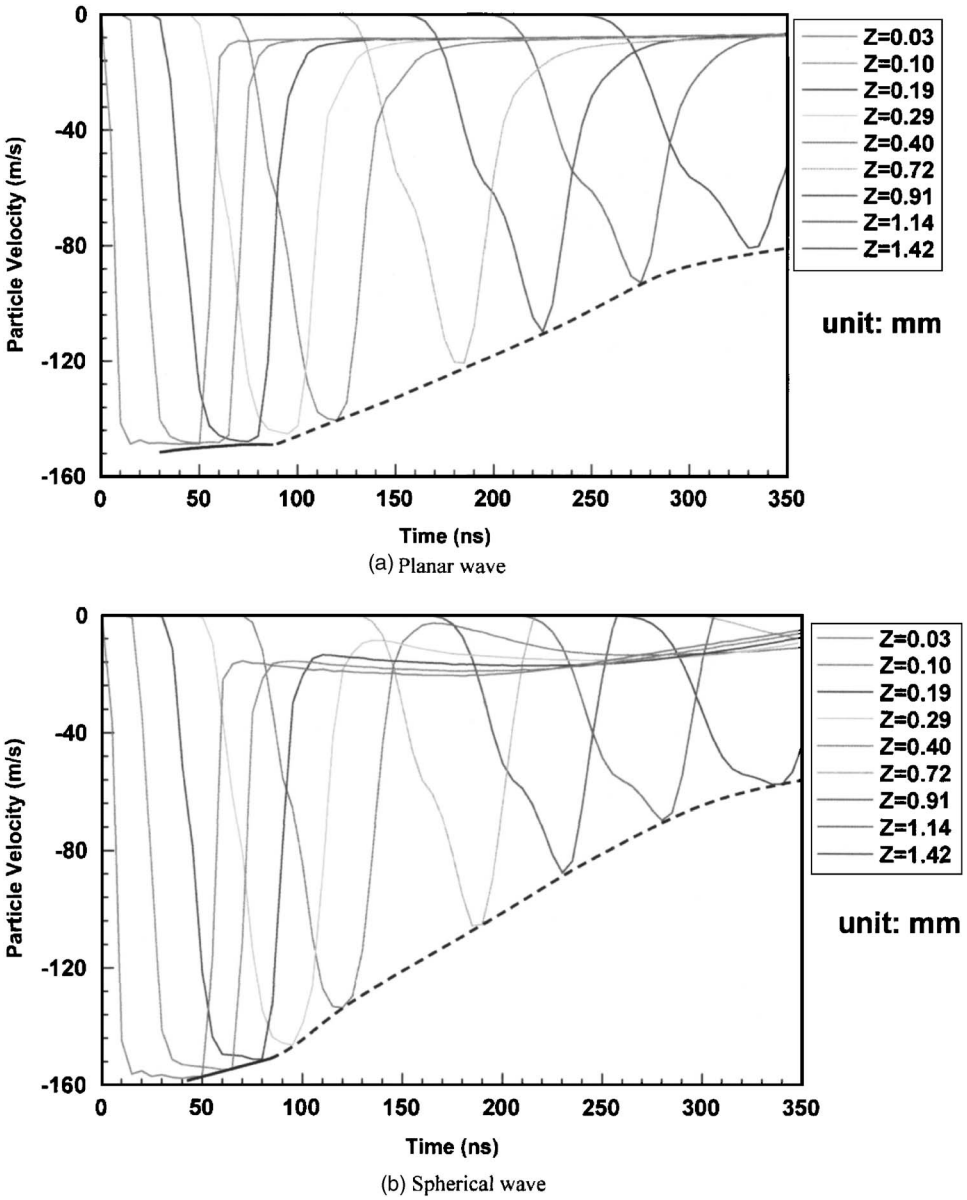

FIG. 15. The simulated attenuation of the particle velocity of shock waves: (a) planar shock wave and (b) spherical shock wave. The laser pulse duration time is 50 ns. When $t=50$ ns, the shock wave already reached at $Z=0.19$ mm, so the loading region is from $Z=0$ mm to $Z\approx 0.2$ mm.

inertial property of media, and meanwhile U and Δx are assumed to be constant, therefore, the value of K_S or K_P is only dependent on ΔP. Clearly, the ΔP during loading is less than that during unloading, therefore, the attenuation during loading is slower than that during unloading. Figure 15 shows the simulated attenuation of a shock wave propagating in the copper plate with a thickness of 1.6 mm, and the loading duration time is 50 ns. It is found that the shock waves decay very slowly near the shocked top surface. The numerical results also demonstrate that for both planar shock wave and spherical shock wave the attenuation during loading is much slower than that during unloading. From the numerical results, the attenuation of the shock wave during loading appears to be linear, and the slope for the planar wave is smaller than that for spherical wave; during unloading the attenuation appears to be exponentially decaying.

The above discussion only considers the attenuation of the shock wave due to geometry and loading conditions. It is known that the attenuation of shock wave is mainly affected by plastic deformation and interaction between rarefaction wave and shock wave.

Note that the velocity near the shocked top surface is about twice the speed at interior locations because the free surface generates a reflected wave traveling in the opposite direction. As in the case of the stress-time profiles, the HEL becomes more discernible with an increase in propagation distance from the shocked top surface. This is due to the fact that the plastic wave propagates slower than the elastic precursor and thus the two waves tend to separate with an increase in propagation distance.

Figure 16 shows that the calculated node speed history at three nodes at the top, the middle and, the bottom of the copper plate in the case of planar shock propagation. The node speed is about twice of the particle velocity when the node is located at the reflection surface (free surface), so Fig. 16 basically demonstrates the attenuation of particle velocity during the propagation.

VI. CONCLUSIONS

A FEM model to simulate shock wave propagation in solids is proposed to calculate induced deformation and re-

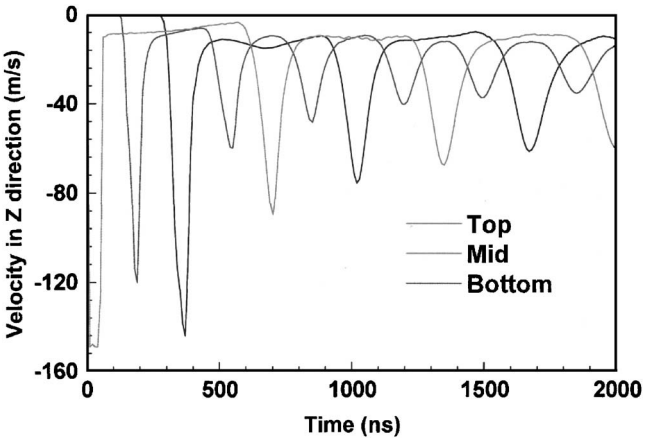

FIG. 16. The calculated node speed history at three nodes in the top, mid, and bottom surfaces for the planar shock case.

sidual stress fields in laser peen forming (LPF) and laser shock peening (LSP). The microscale LPF process has been numerically and experimentally studied in this work. The experimental measurement of deformation and residual stress fields showed a good agreement with the numerical results. Based on this model, the variation of shock wave velocity and attenuation in LPF and LSP are further analyzed, respectively. Both analytical and numerical results show that shock wave velocity is affected by equivalent plastic strain when the shock wave is in the plastic regime, and that attenuation of shock waves in LPF and LSP is dependent on loading states. Those results can be very useful in exploring and designing applications of LPF and LSP.

ACKNOWLEDGMENT

The authors gratefully acknowledge the assistance in x-ray-microdiffraction experiments from Dr. J. L. Jordan-Sweet, Brookhaven National Laboratory.

APPENDIX

A centered single shock wave is propagating, as shown in Fig. 14. The center of the shock wave is at x with pressure P, and the leading and tailing edges of the shock are at $(x+\Delta x/2)$ and $(x-\Delta x/2)$ with pressures of $(P+\Delta P/2)$ and $(P-\Delta P/2)$, respectively. The width of the shock wave at x is Δx. When the shock wave moves to $(x+dx)$, the location x_+ of the leading edge can be expressed as

$$x_+ = x + \Delta x/2 + \left(\frac{\partial U}{\partial P}\frac{\Delta P}{2}\right)\frac{dx}{U}. \tag{A1}$$

Meanwhile, the location x_- of the tailing edge is

$$x_- = x - \Delta x/2 + \left(-\frac{\partial U}{\partial P}\frac{\Delta P}{2}\right)\frac{dx}{U}, \tag{A2}$$

where $\Delta P = P(x+\Delta x/2) - P(x-\Delta x/2)$. Therefore, the location of the center of the shock wave at $(x+dx)$ can be expressed as the following:

$$\Delta x(x+dx) = x_+ - x_- = \Delta x(x) + \frac{\partial U}{\partial P}\frac{\Delta P dx}{U}, \tag{A3}$$

or

$$\frac{d\Delta x}{dx} \approx \frac{\Delta x(x+dx) - \Delta x(x)}{dx} = \frac{\partial U}{\partial P}\frac{\Delta P}{U}. \tag{A4}$$

If only considering kinematic energy of the shock wave, energy conservation for a planar shock wave gives

$$\Delta x u^2 = \text{const}. \tag{A5}$$

While for a spherical shock wave, energy conservation yields

$$x^2 \Delta x u^2 = \text{const}. \tag{A6}$$

Differentiating Eqs. (A5) and (A6), respectively, leads to

$$\frac{du}{dx} = -\frac{u d\Delta x}{2\Delta x dx} \quad \text{(planar wave)}, \tag{A7}$$

$$\frac{du}{dx} = -\frac{u}{x}\left(1 + \frac{x d\Delta x}{2\Delta x dx}\right) \quad \text{(spherical wave)}. \tag{A8}$$

Substituting Eq. (A4) into Eqs. (A7) and (A8), respectively, yields

$$\frac{du}{dx} = -uK_P \quad \text{(planar wave)}, \tag{A9}$$

$$\frac{du}{dx} = -\frac{u}{x}(1 + xK_S) \quad \text{(spherical wave)}, \tag{A10}$$

where $K_S = K_P = 1/2\Delta x(\partial U/\partial P)\Delta P/U$. K_S and K_P are relative to U, P, and Δx. If the shock wave propagates a short distance from x_0 to x, K_S and K_P can be approximately assumed to be constant. Thus, integrating Eqs. (A9) and (A10) yields Eqs. (16) and (17).

[1] J. A. Fox, Appl. Phys. Lett. **24**, 461 (1974).
[2] A. H. Clauer and J. H. Holbrook, *Shock Waves and High Strain Phenomena in Metals–Concepts and Applications* (Plenum, New York, 1981), p. 675.
[3] P. Peyre, A. Sollier, I. Chaieb, L. Berthe, E. Bartnicki, C. Braham, and R. Fabbro, Eur. Phys. J.: Appl. Phys. **23**, 83 (2003).
[4] W. Zhang and Y. L. Yao, in Proceedings of the 19th International Congress on Applications of Lasers and Electro-Optics, Detroit, MI, 1–5 October 2000 (unpublished), pp. E183–192.
[5] W. Zhang and Y. L. Yao, ASME J. Manuf. Sci. Eng. **124**, 369 (2002).
[6] L. Berth, R. Fabbro, P. Peyre, L. Tollier, and E. Bartnicki, J. Appl. Phys. **82**, 2826 (1997).
[7] R. Fabbro, J. Fournier, P. Ballard, D. Devaux, and J. Virmont, J. Appl. Phys. **68**, 775 (1990).
[8] M. Zhou, Y. Zhang, and L. Cai, J. Appl. Phys. **91**, 5501 (2002).
[9] T. Wang and M. J. Platts, J. Mater. Process. Technol. **122**, 374 (2002).
[10] K. Ding and L. Ye, Surf. Eng. **19**, 127 (2003).
[11] C.-H. Mok, J. Appl. Phys. **39**, 2072 (1968).
[12] A. Caruso, S. Y. Guskov, I. Y. Doskach, N. V. Zmitrenko, V. B. Rozanov, and C. Strangio, Proc. SPIE **4424**, 508 (2001).
[13] F. Cottet and M. Boustie, J. Appl. Phys. **66**, 4067 (1989).
[14] J. L. Ocana, M. Morales, C. Molpeceres, and J. Torres, Appl. Surf. Sci. **238**, 242 (2004).
[15] V. K. Senecha, J. Zhang, W. Wang, and H. C. Pant, J. Phys.: Condens. Matter **14**, 10917 (2002).
[16] W. Zhang and Y. L. Yao, J. Manuf. Process. **3**, 128 (2001).
[17] V. E. Fortov, V. V. Kostin, and S. Eliezer, J. Appl. Phys. **70**, 4524 (1991).
[18] M. H. Rice, R. G. McQueen, and J. M. Walsh, "Compression of Solids by

Strong Shock Wave," in Solid State Physics, edited by F. Seitz and D. Turnbull (Academic Press, New York, 1958), p. 42.
[19]J. VonNumann and R. D. Richtmyer, J. Appl. Phys. **21**, 232 (1950).
[20]J. R. Assay and M. Shahipoor, *High-Pressure Shock Compression of Solids* (Springer-Verlag, New York, 1992), p. 8.
[21]*ABAQUS User's Manual, Version 6.2* (Hibbitt, Karlsson and Sorensen, Inc., Pawtucket, RI, 1998).
[22]G. R. Johnson, J. M. Hoegfeldt, U. S. Lindholm, and A. Nagy, J. Eng. Mater. Technol. **105**, 42 (1983).
[23]D. J. Steinberg, S. G. Cochran, and M. W. Guinan, J. Appl. Phys. **51**, 1498 (1980).
[24]B. D. Cullity, *Elements of X-Ray Diffraction*, 2nd ed. (Addison-Wesley, London, 1978), pp. 268–270.
[25]T. Ungar, G. Ribarik, J. Gubicza, and P. Hanuk, Acta Metall. **32**, 332 (1984).
[26]L. M. Barker and R. E. Hollenbach, J. Appl. Phys. **45**, 4872 (1974).
[27]J. Lipkin and J. R. Asay, J. Appl. Phys. **48**, 182 (1977).